

Article

Lateral Buckling of Subsea Pipelines Triggered by Sleeper with a Nonlinear Pipe–Soil Interaction Model

Zhenkui Wang ^{1,2}  and C. Guedes Soares ^{2,*} 

¹ Ocean College, Zhejiang University, Zhoushan 316021, China; zhenkui.wang@zju.edu.cn

² Centre for Marine Technology and Ocean Engineering (CENTEC), Instituto Superior Técnico, Universidade de Lisboa, 1049-001 Lisbon, Portugal

* Correspondence: c.guedes.soares@centec.tecnico.ulisboa.pt

Abstract: Buckle-initiation techniques, such as sleepers, are usually installed to trigger lateral buckling at pre-designated locations to release the axial compressive forces induced by thermal loading. Taking the nonlinear pipe–soil interaction model into account, a mathematical model is proposed to investigate the lateral buckling of subsea pipelines triggered by a sleeper. The numerical solution is validated by comparing the model with solutions in the literature, and the model shows good agreement. The discrepancy between them is analysed by presenting the effect of mobilisation distance during buckling. The influence of the breakout resistance, sleeper height, and sleeper friction coefficient on the buckled configuration, post-buckling behaviour, and minimum critical temperature difference is discussed parametrically. The results show that the deformation of the buckled pipeline shrinks, and both the minimum critical temperature difference and the maximum stress along the buckled pipeline enlarge when the nonlinear pipe–soil interaction model is incorporated. However, the influence of the nonlinear pipe–soil interaction reduces with increasing sleeper height.

Keywords: subsea pipeline; nonlinear pipe–soil interaction model; breakout resistance; sleeper



Citation: Wang, Z.; Guedes Soares, C. Lateral Buckling of Subsea Pipelines Triggered by Sleeper with a Nonlinear Pipe–Soil Interaction Model. *J. Mar. Sci. Eng.* **2022**, *10*, 757. <https://doi.org/10.3390/jmse10060757>

Academic Editor: Fuping Gao

Received: 22 April 2022

Accepted: 22 May 2022

Published: 30 May 2022

Publisher's Note: MDPI stays neutral with regard to jurisdictional claims in published maps and institutional affiliations.



Copyright: © 2022 by the authors. Licensee MDPI, Basel, Switzerland. This article is an open access article distributed under the terms and conditions of the Creative Commons Attribution (CC BY) license (<https://creativecommons.org/licenses/by/4.0/>).

1. Introduction

Subsea pipelines may buckle laterally due to the excessive axial compressive force due to high-temperature and high-pressure conditions. Lateral buckling occurs when the axial compressive force reaches critical levels. Lateral buckling, if not controlled, can lead to serious accidents involving local buckling, fracture, and fatigue [1]. To control this phenomenon, buckle initiation techniques, such as sleepers, are employed along pipelines to trigger buckles at predesigned locations. A sleeper is a pipe segment that is installed underneath and perpendicular to the pipeline, which typically has a low friction surface to reduce the lateral friction force. Thus, the pipeline is uplifted vertically. A combination of the vertical out-of-straightness and low lateral resistance results in reduced critical buckling force. When the sleeper is used as the buckle initiation facility, part of the pipeline is suspended. The pipeline segment at the end of the suspended section has a larger embedment into the seabed, since a vertical concentrated force exists. This embedment affects the lateral breakout resistance, which is a key design parameter governing the initiation of the lateral buckle. Thus, a nonlinear pipe–soil interaction model is considered in the mathematical model to investigate the influence of breakout resistance on post-buckling behaviour.

The global buckling of subsea pipelines was investigated by numerous researchers. Hobbs' solutions for a straight pipeline were derived by assuming specific buckling mode shapes and constant lateral soil resistance [2]. Based on this, an analytical model was proposed by Taylor and Gan [3] with a consideration of initial imperfection. A simplified analytical model was proposed by Croll [4] for upheaval buckling. The interaction between propagation buckling and global buckling in subsea pipelines was investigated

by Karampour et al. [5]. This interaction leads to a significant reduction in buckle design capacity. The lateral buckling of imperfect pipelines was studied by Liu et al. [6], using FEM. The analytical solutions for the high-order lateral buckling of a pipeline with symmetric and anti-symmetric initial imperfection were derived by Hong et al. [7] and Liu et al. [8], respectively. Lateral buckling was investigated by Konuk [9,10] with coupled lateral and axial pipe–soil interactions. Zhang et al. [11,12] derived unified formulas for the critical buckling forces of the upheaval and lateral buckling of subsea pipelines with different types of initial imperfection. The influence of the pipe length on the lateral buckling behaviour of imperfect pipelines was investigated through FEM [13].

More recently, researchers investigated the influence of the nonlinear pipe–soil interaction model on lateral buckling. Zeng and Duan [14] used a quintic polynomial formula to simulate nonlinear pipe–soil interactions. Incorporating the tri-linear pipe–soil interaction model, Chee et al. [15] investigated the effect of imperfections on the buckling response through FEM. Considering both the initial imperfection and the nonlinear lateral soil resistance model, the critical force of the lateral buckling was analysed by assuming that the length of the buckled region equals the wavelength of initial imperfection [16].

To increase the reliability of buckle formation predictions, buckle initiation facilities were incorporated into the mathematical models. A single buoyancy or distributed buoyancy with a specific length installed along the pipeline was considered to derive some simple analytical solutions [17]. The critical load of lateral buckling triggered by a single buoyancy was investigated by Shi and Wang [18]. Moreover, dual distributed buoyancy sections with a gap between them were employed to initiate lateral buckling [19]. A new way to trigger lateral buckling is to introduce a pre-deformed section along the pipeline before installation [20]. Lateral buckling triggered by a sleeper was investigated experimentally by Silva-Junior et al. [21] and de Oliveira Cardoso and Solano [22]. Bai et al. [23] studied the lateral buckling triggered by dual sleepers through FEM. Analytical solutions for antisymmetric buckling modes triggered by a sleeper were obtained by Wang and Tang [24]. They found that the symmetric buckling mode was more likely to occur with lower sleeper friction or smaller sleeper height. Hong and Liu [25] investigated the vertical deflection of a pipeline on a sleeper by FEM.

By assuming constant lateral soil resistance, analytical solutions were derived for the lateral thermal buckling triggered by a sleeper in [26]. In practice, the pipeline always has an initial embedment into the soil and the lateral soil resistance is not constant. However, there are no studies about lateral thermal buckling triggered by sleepers that consider nonlinear lateral soil resistance.

The innovative aspect of this study is the nonlinear pipe–soil interaction model that is incorporated into the governing equations. In previous published studies about lateral buckling triggered by sleepers, the lateral soil resistance, $f(w_2)$, is assumed to be constant. However, in this study, this function is nonlinear and it includes the effect of breakout resistance. This is due to the fact that in practice, pipe–soil interactions are nonlinear.

2. Mathematical Modelling

To avoid rogue buckles along subsea pipelines, buckle-initiation techniques, such as installing sleepers along the pipeline, are usually employed to trigger the pipeline to buckle in a controlled way at the predesignated location. For a pipeline laid on a sleeper and subjected to a temperature difference T_0 , the axial compressive force is accumulated. The axial compressive force, P_0 , is expressed as

$$P_0 = EA\alpha T_0 \quad (1)$$

where E is the elastic modulus, A is the cross-sectional area of the pipeline, and α is the coefficient of linear thermal expansion.

When P_0 is larger than the critical value, lateral buckling can be triggered at sleeper. The configuration and load distribution of lateral buckling are illustrated in Figure 1. From Figure 1a, it is clear that part of the pipe segment within $-l_1 \leq x \leq l_1$ is uplifted by the

sleeper. In $-l_1 \leq x \leq l_1$, the soil resistances are zero. However, there are concentrated contact forces F_s between pipeline and sleeper at the sleeper and F_t between the pipe and seabed at the end of the suspended section, respectively. The vertical configuration of the pipeline laid on a sleeper was solved by Wang et al. [26]. From their derivation, F_s and F_t can be expressed as

$$F_s = \frac{4}{3}W_{pipe}l_1 \text{ and } F_t = \frac{1}{3}W_{pipe}l_1 \tag{2}$$

where W_{pipe} is the submerged weight per unit length and l_1 is the half-length of the free span, solved by

$$l_1 = \sqrt[4]{\frac{72EIv_{om}}{W_{pipe}}} \tag{3}$$

where I is the moment of inertia and v_{om} is the sleeper height. Therefore, the value of l_1 can be obtained by Equation (3) when v_{om} is specified. Furthermore, F_s and F_t can be solved.

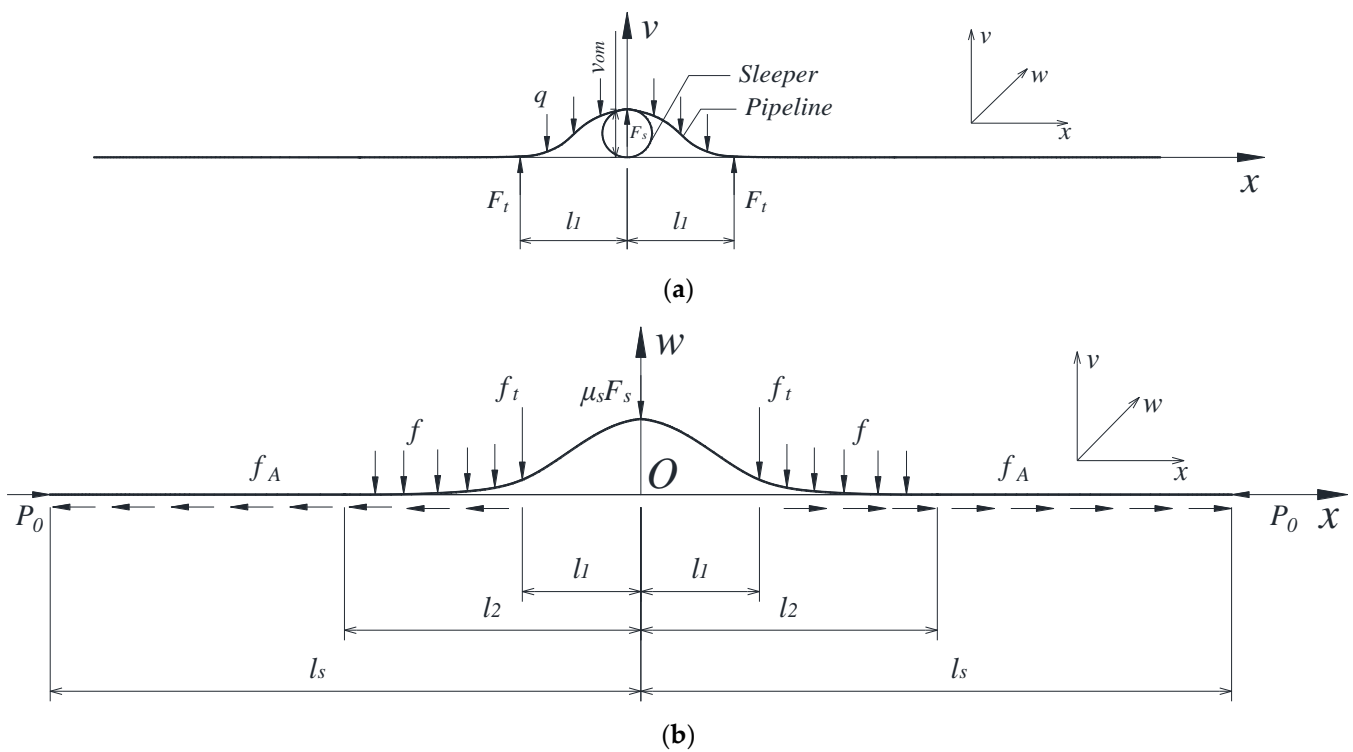


Figure 1. Configuration and load distribution. (a) Vertical plane. (b) Horizontal plane.

After the pipeline buckles, additional pipe coming from the thermal expansion is fed into the buckled section. Therefore, the axial force reduces partially due to the release of axial strain (see Figure 2). The axial force within the suspended region $-l_1 < x < l_1$, denoted by P , is constant. At $x = \pm l_1$, there is a jump in axial force with an amplitude of f_{At} induced by F_t . Within the region where the pipeline makes contact with the seabed, the axial force increases because of the restraint of axial soil resistance. The axial force will reach P_0 at $x = \pm l_s$. From Figure 2, the axial force distribution $\bar{P}(x)$ is

$$\bar{P}(x) = \begin{cases} P & (0 \leq x < l_1) \\ P + f_{At} + f_A(x - l_1) & (l_1 \leq x \leq l_s) \end{cases} \tag{4}$$

where $f_A = \mu_A W_{pipe}$ is the axial soil resistance per unit length and μ_A is the axial friction coefficient. The force $f_{At} = \mu_A F_t$ is induced by F_t .

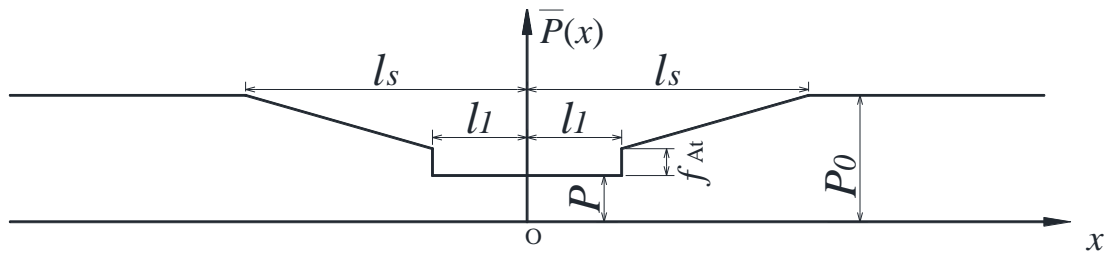


Figure 2. Axial compressive force distribution.

The axial force at $x = l_s$ is

$$\bar{P}(l_s) = P_0 = P + f_{At} + f_A(l_s - l_1) \tag{5}$$

Linear beam theory is used to simulate pipeline buckling. Thus, the equilibrium equations governing lateral deformation are [27]:

$$\begin{cases} EI \frac{d^4 w_1}{dx^4} + P \frac{d^2 w_1}{dx^2} = 0 & (0 \leq x < l_1) \\ EI \frac{d^4 w_2}{dx^4} + \bar{P}(x) \frac{d^2 w_2}{dx^2} = -f(w_2) & (l_1 \leq x \leq l_2) \end{cases} \tag{6}$$

where w_1 and w_2 are lateral deflections, EI is bending stiffness, and $f(w_2)$ is the nonlinear lateral soil resistance determined by the nonlinear pipe–soil interaction model, as shown in Figure 3. Here, the variation in the axial force within the buckled region $l_1 \leq x \leq l_2$ is ignored when solving lateral deformations. This assumption is acceptable [26,28].

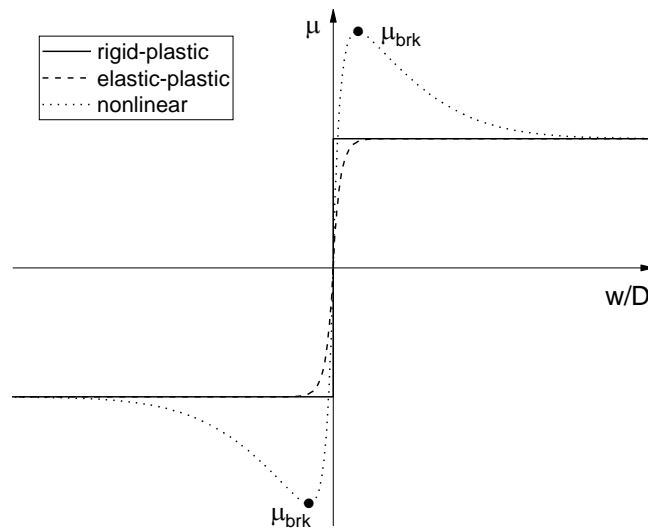


Figure 3. Pipe–soil interaction models.

Here, the nonlinear pipe–soil interaction model proposed by Chatterjee et al. [29] is employed. It can simulate breakout resistance and is given by

$$\mu = \frac{w}{|w|} \left(\mu_{brk} \left(1 - e^{-a_1 \left(\frac{|w|}{D} \right)^{a_2}} \right) + (\mu_{res} - \mu_{brk}) \left(1 - e^{-a_3 \left(\frac{|w|}{D} \right)^{a_4}} \right) \right) \tag{7}$$

where μ , μ_{brk} and μ_{res} are the equivalent friction coefficients, and D is the external diameter of the pipeline. The quantities $f(w) = \mu W_{pipe}$, $F_{brk} = \mu_{brk} W_{pipe}$ and $F_{res} = \mu_{res} W_{pipe}$ are,

therefore, respectively, the nonlinear lateral soil resistance, the breakout resistance, and the residual resistance. The value of the coefficient a_3 in [29] is given as

$$a_3 = a_5 \left(\frac{W_{pipe}}{V_{max}} \right) + a_6 \tag{8}$$

where W_{pipe} is the weight of the pipe and V_{max} is the vertical bearing capacity. The values of a_5 and a_6 are calculated by

$$a_5 = 8.2 \frac{v_{init}}{D} - 4.9, \quad a_6 = -5.8 \frac{v_{init}}{D} + 4.5 \tag{9}$$

where v_{init} is the initial embedment of the pipe into the soil. In [29], $a_1 = 25$ and $a_4 = 1.5$ are employed, but $a_2 = 1$ is used here in order to have a finite linear resistance, which is physically realistic. $V_{max} = 5W_{pipe}$ and $v_{init} = 0.3D$ are adopted so that $a_3 = 2.272$, and set $\mu_{res} = 0.5$.

Due to symmetry, half a pipeline is considered. The slope of the deflection at $x = 0$ is zero, while the shear force $f_{ow} = \mu_s F_s / 2$ at $x = 0$ is induced by the friction force $\mu_s F_s$. Here, μ_s is the friction coefficient between pipeline and sleeper. The displacement, slope, and moment at $x = l_2$ are also zero. The boundary conditions at $x = 0$ and $x = l_2$ are

$$\begin{cases} \frac{dw_1}{dx}(0) = 0 \\ \frac{d^3w_1}{dx^3}(0) + \frac{f_{ow}}{EI} = 0 \\ w_2(l_2) = 0 \\ \frac{dw_2}{dx}(l_2) = 0 \\ \frac{d^2w_2}{dx^2}(l_2) = 0 \end{cases} \tag{10}$$

The displacement, slope, and bending moment must be continuous at the touchdown point $x = l_1$, while there is a jump in shear force with an amplitude of $f_t = \mu_{res} F_t$ at $x = l_1$ induced by the force F_t . Thus, additional conditions at $x = l_1$ are

$$\begin{cases} w_1(l_1) = w_2(l_1) \\ \frac{dw_1}{dx}(l_1) = \frac{dw_2}{dx}(l_1) \\ \frac{d^2w_1}{dx^2}(l_1) = \frac{d^2w_2}{dx^2}(l_1) \\ \frac{d^3w_1}{dx^3}(l_1) = \frac{d^3w_2}{dx^3}(l_1) + \frac{f_t}{EI} \end{cases} \tag{11}$$

With Equations (10) and (11), the nonlinear governing equations are solved numerically by the shooting method [30]. Once the lateral deflections are known, the geometric shortening u_2 is obtained by

$$u_2 = \frac{1}{2} \int_0^{l_1} \left(\frac{dw_1}{dx} \right)^2 dx + \frac{1}{2} \int_{l_1}^{l_2} \left(\frac{dw_2}{dx} \right)^2 dx \tag{12}$$

The following compatibility condition is employed to link the lateral deflection and the thermal loading induced deflection:

$$u_1 = u_2 \tag{13}$$

where u_1 is thermal expansion in $0 < x < l_s$.

We have

$$u_1 = \int_0^{l_s} \frac{\Delta \bar{P}(x)}{EA} dx \tag{14}$$

where $\Delta \bar{P}(x) = P_0 - \bar{P}(x)$.

Thus, this leads to

$$u_1 = \frac{f_A(l_s - l_1)^2}{2EA} + \frac{(P_0 - P)l_1}{EA} \tag{15}$$

The following formula is obtained by combining Equations (5), (13), and (15).

$$l_s = \sqrt{\frac{1}{3}l_1^2 + \frac{2EAu_2}{f_A}} \tag{16}$$

With Equations (5) and (16), one finally obtains

$$P_0 = P + f_A \left(\sqrt{\frac{1}{3}l_1^2 + \frac{2EAu_2}{f_A}} - \frac{2}{3}l_1 \right) \tag{17}$$

The bending moment is obtained by

$$M = EI \frac{d^2w}{dx^2} \tag{18}$$

where w stands for w_1 or w_2 , and the bending stress σ_M is

$$\sigma_M = \frac{MD}{2I} \tag{19}$$

The maximum stress is

$$\sigma_m = \sigma_P + \sigma_{Mm} \tag{20}$$

where the stresses σ_P and σ_{Mm} , induced by axial force P and maximum bending moment M_m , respectively, are

$$\begin{cases} \sigma_P = \frac{P}{A} \\ \sigma_{Mm} = \left| \frac{M_m D}{2I} \right| \end{cases} \tag{21}$$

3. Results

The mathematical model is validated by comparing it with the analytical solution in [26], and the discrepancy between them is discussed. Next, the influence of μ_{brk} , v_{om} and μ_s is analysed. The results are obtained by employing the analytical formulation developed in Section 2 and taking the parameters in Table 1.

Table 1. Parameters.

Parameter	Value	Unit
External diameter D	323.9	mm
Wall thickness t	12.7	mm
Elastic modulus E	206	GPa
Steel density ρ	7850	kg/m ³
Coefficient of thermal expansion α	1.1×10^{-5}	°C
Axial friction coefficient μ_A	0.5	—

One should note that only the analytical solutions in Figures 4 and 5 come from [26], which is used to validate the numerical results obtained in this study. In [26], the lateral soil resistance is assumed to be constant, while in the present study, nonlinear lateral soil resistance is considered. Moreover, in [26], analytical solutions are obtained due to the assumption of constant lateral soil resistance. In the present study, because the lateral soil resistance is nonlinear, Equation (6) cannot be solved analytically. Thus, the shooting method is used to solve Equation (6) to obtain the numerical results.

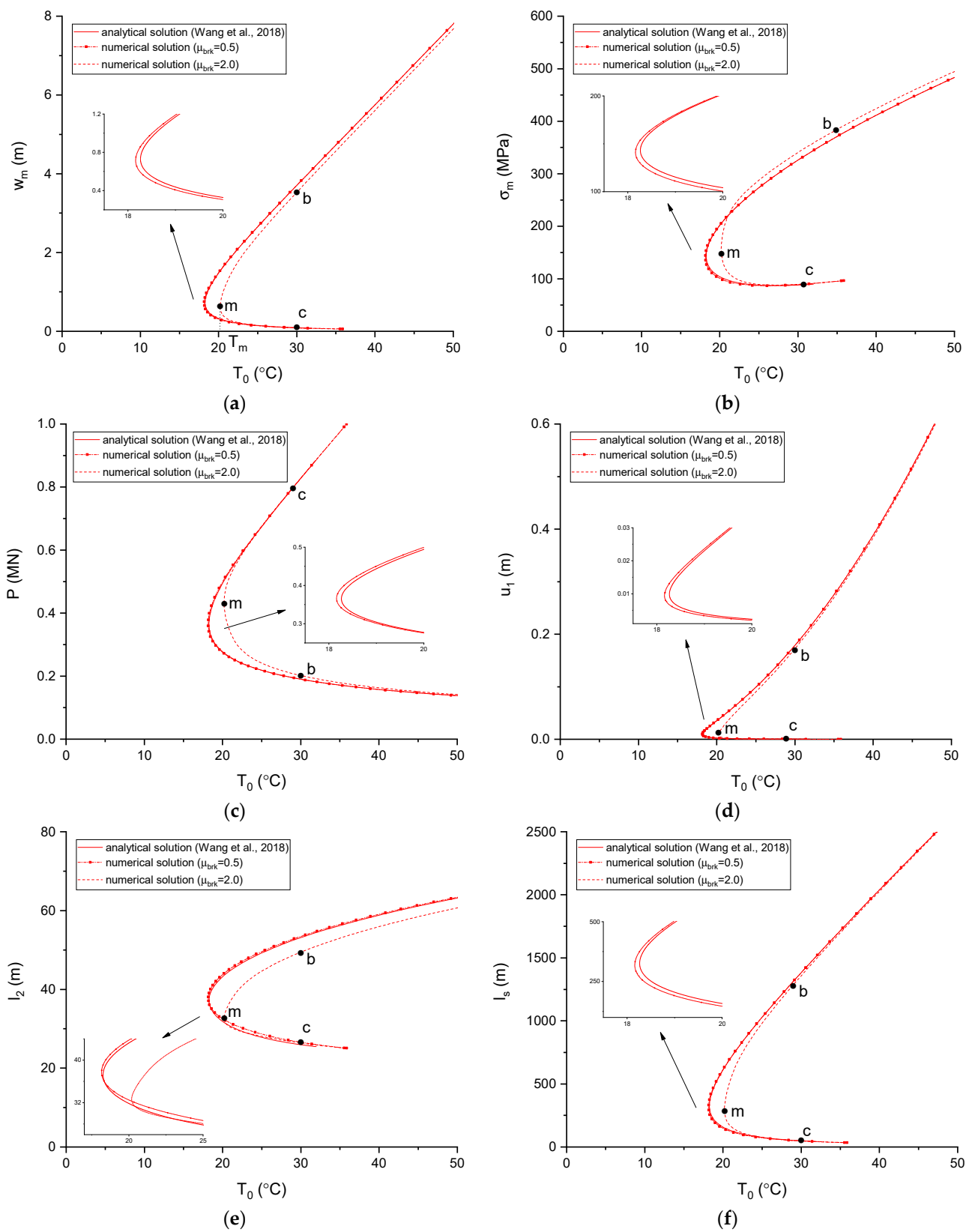


Figure 4. Validation. (a) Displacement amplitude w_m . (b) Maximum stress σ_m . (c) Axial force P . (d) Thermal expansion u_1 . (e) Half-length of buckled region l_2 . (f) Half-length of feed-in region l_s . ($v_{om} = 0.1$ m, $\mu_s = 0.1$) [26].

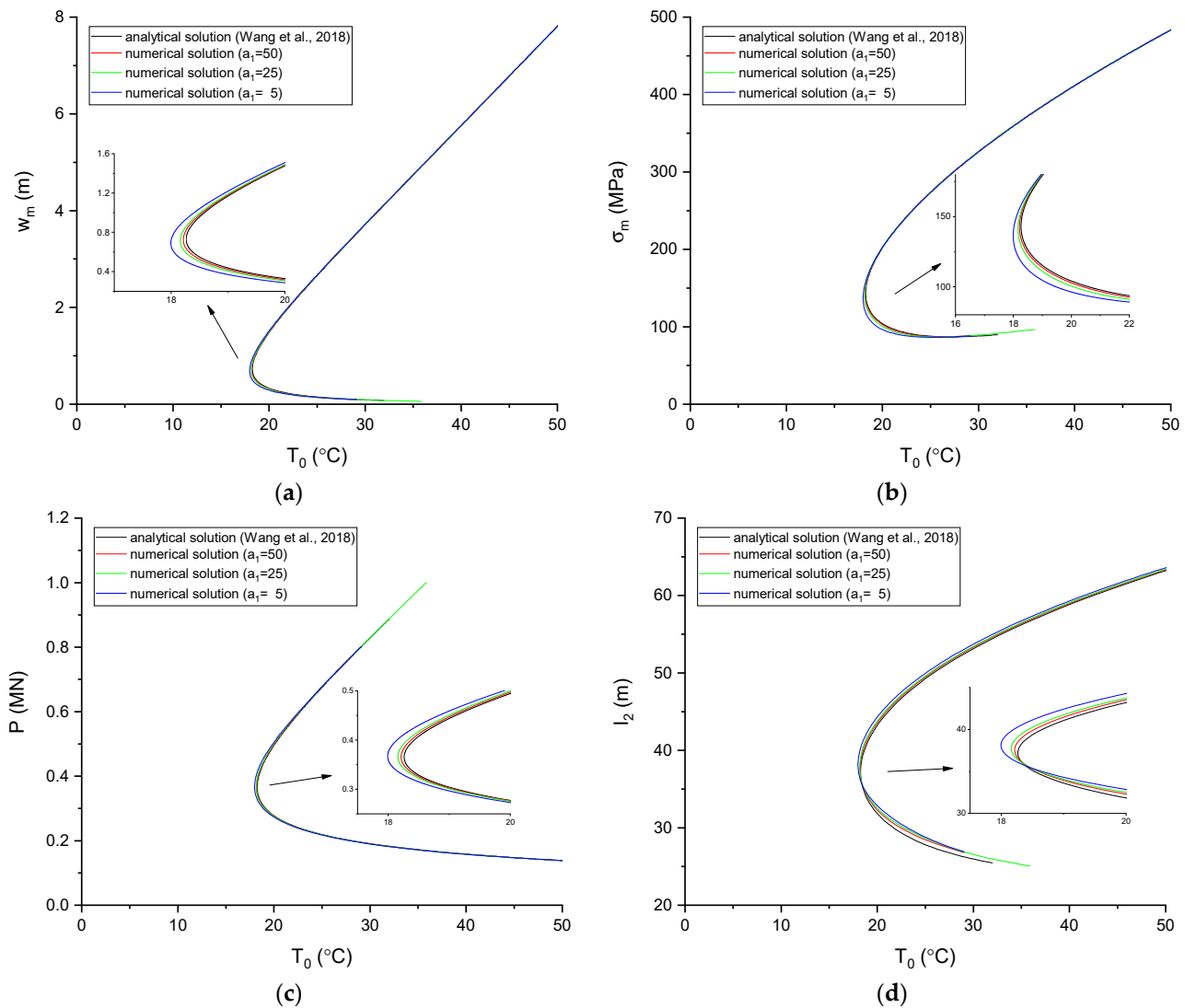


Figure 5. Error analysis. (a) w_m . (b) σ_m . (c) P . (d) l_2 ($\mu_{brk} = 0.5$, $v_{om} = 0.1$ m, $\mu_s = 0.1$) [26].

3.1. Validation

The solutions obtained in this study were validated by comparing them with the analytical solutions in [26], as shown in Figure 4. An error analysis is shown in Figure 5. In Figure 4, the analytical solutions are obtained by using the formulas derived in Wang et al. [26] with constant lateral soil resistance. To compare with the analytical solutions, the numerical solutions shown in Figure 4 are obtained by assuming $\mu_{brk} = 0.5$. For $\mu_{brk} = 0.5$, the non-linear pipe–soil interaction model is reduced to elastic–plastic (see Figure 3). The numerical solutions for $\mu_{brk} = 2.0$ are also illustrated in Figure 4 to show the influence of the nonlinear pipe–soil interaction.

In Figure 4, there are two branches for each solution, which are denoted as **m-b** and **m-c**. The temperature difference at m , i.e., T_m , is called the minimum critical temperature difference, since solutions only exist for $T_0 > T_m$.

From Figure 4, the numerical solutions for $\mu_{brk} = 0.5$ are in good agreement with the analytical solutions, except that there is a slight discrepancy between them around T_m . This discrepancy comes from the difference in mobilization distance. For the rigid–plastic model, the resistance is always constant (see Figure 3). For the elastic–plastic model, the lateral soil resistance increases from zero to residual resistance gradually (see Figure 3).

In Figure 4, the discrepancy between the analytical and numerical solutions reduces as the temperature difference increases. The reason for this is that the displacement amplitude

increases along with the temperature difference, so that more pipe sections fall into the region of constant lateral soil resistance for numerical solutions.

A more detailed error analysis is illustrated in Figure 5. Figure 6 shows that the mobilization distance is controlled by the parameter a_1 . The mobilization distance is the distance that the lateral resistance reaches μ_{brk} . In Figure 6, $\mu_{brk} = \mu_{res} = 0.5$, so the mobilization distance in Figure 6 is the distance at which μ reaches 0.5. The elastic-plastic model approaches the rigid-plastic model for larger a_1 , since the mobilization distance becomes smaller. In Figure 5, the discrepancy between the analytical and numerical solutions becomes smaller for larger a_1 . In Figures 4 and 5, the discrepancy in half-buckled length l_2 is larger than in the other parameters. This is because the deflection at the ends of the buckled section is small, and it is affected by the mobilization distance. For the remaining parameters, the discrepancy between the analytical and numerical solutions is small enough.

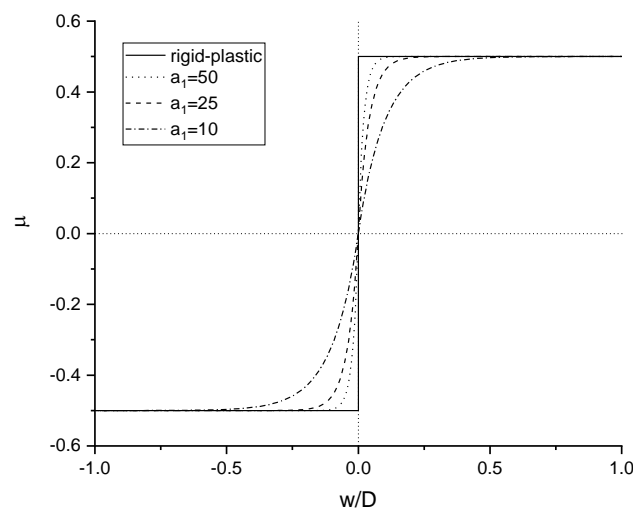


Figure 6. Pipe–soil interaction model with different a_1 .

In Figure 4a, T_m becomes larger when the nonlinear pipe–soil interaction model is considered, which means that lateral buckling can only be triggered at higher temperature differences. At the same temperature difference, both w_m and l_2 become smaller when considering the nonlinear pipe–soil interaction model (see Figure 4a,e). Thus, the use of an additional pipe to create lateral deflection, which comes from thermal expansion, also reduces (see Figure 4d), so that l_s decreases, as shown in Figure 4f. However, P within the buckled section becomes larger due to the restriction of the breakout resistance. Moreover, at the same temperature difference, the maximum stress σ_m becomes larger when nonlinear pipe–soil interaction is considered. This means that the maximum stress is underestimated when assuming the lateral soil resistance to be constant.

3.2. Parametric Study

3.2.1. Influence of μ_{brk}

The influence of μ_{brk} on the buckled configuration, post-buckling behaviour, and minimum critical temperature difference T_m is shown in Figures 7–9, respectively.

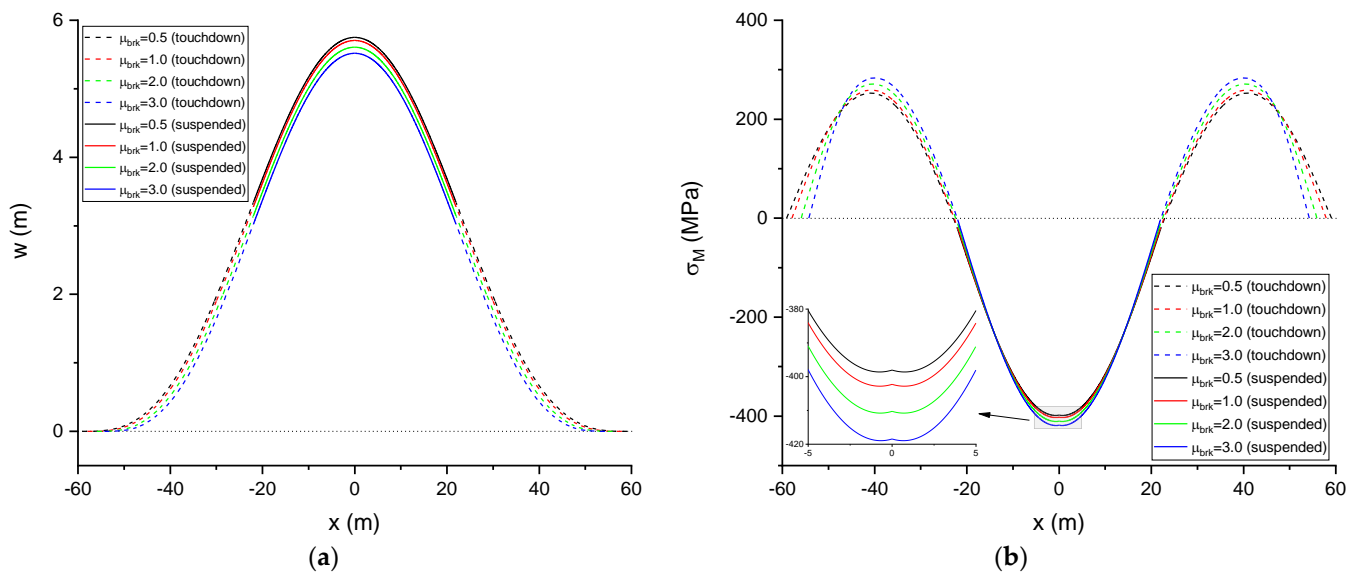


Figure 7. Influence of μ_{brk} on configurations. (a) Deformed shapes. (b) Bending stresses ($v_{om} = 0.1$ m, $\mu_s = 0.1$, $T_0 = 40$ °C).

In Figure 7, the dashed curves are the pipe sections in contact with the seabed, and the solid curves are the pipe sections suspended due to the existence of the sleeper. In Figure 7a, both the touchdown and suspended pipe segments shrink with larger μ_{brk} . In Figure 7b, there are two extrema of bending stress in the positive direction. Another three extrema of bending stress occur around the sleeper. One local minimum (absolute value) of bending stress appears at the sleeper, while there are two other local maxima (absolute value) of bending stress close to the sleeper. The occurrence of the local minimum (absolute value) of bending stress at the sleeper is induced by the friction force between the pipeline and the sleeper. For each specific μ_{brk} , the maximum bending stress is located at the local maxima (absolute value) of bending stress close to the sleeper. For larger μ_{brk} , all the extrema of bending stress in both positive and negative directions become larger.

In Figure 8a, T_m is larger for larger μ_{brk} . A more detailed analysis on the influence of μ_{brk} on T_m is shown in Figure 9, which shows that T_m increases with increasing μ_{brk} for specific values of v_{om} and μ_s , and the increasing rate of T_m reduces with the increase in μ_{brk} . In Figure 9a, under the same μ_{brk} , T_m is larger for smaller v_{om} . The increasing rate of T_m with increasing μ_{brk} is also larger for smaller v_{om} . The reason is that since there are less length of suspended pipeline and larger length of touchdown pipeline with the smaller v_{om} , the breakout resistance has a larger influence on the initiation of lateral buckling. In Figure 9b, under the same μ_{brk} , T_m becomes larger for larger μ_s . The increase in the rate of T_m along with the increasing μ_{brk} remains almost the same for different values of μ_s . The reason for this is that the friction force between the pipeline and the sleeper becomes larger for larger μ_s ; however, the value of μ_s has no influence on the lengths of the suspended or touchdown pipeline segments.

In Figure 8a,e, both the displacement amplitude w_m and the half-buckled length l_2 increase with the increasing T_0 , and need more thermal expansion u_1 to form the buckled deflection (see Figure 8d). Thus, larger l_s is required for larger T_0 , as shown in Figure 8f. The maximum stress also increases with increasing T_0 (see Figure 8b) since large deflection occurs; however, the axial force P reduces with increasing T_0 (see Figure 8c).

In Figure 8a,e, at a specific temperature difference, both w_m and l_2 become smaller for larger μ_{brk} . The reason for this is that since the breakout resistance is larger for larger μ_{brk} , the pipeline is subjected to greater lateral soil resistance. The deflection shrinks with larger μ_{brk} , as shown in Figure 7a. Therefore, both u_1 and l_s become smaller with larger μ_{brk} at the same temperature difference (see Figure 8d,f).

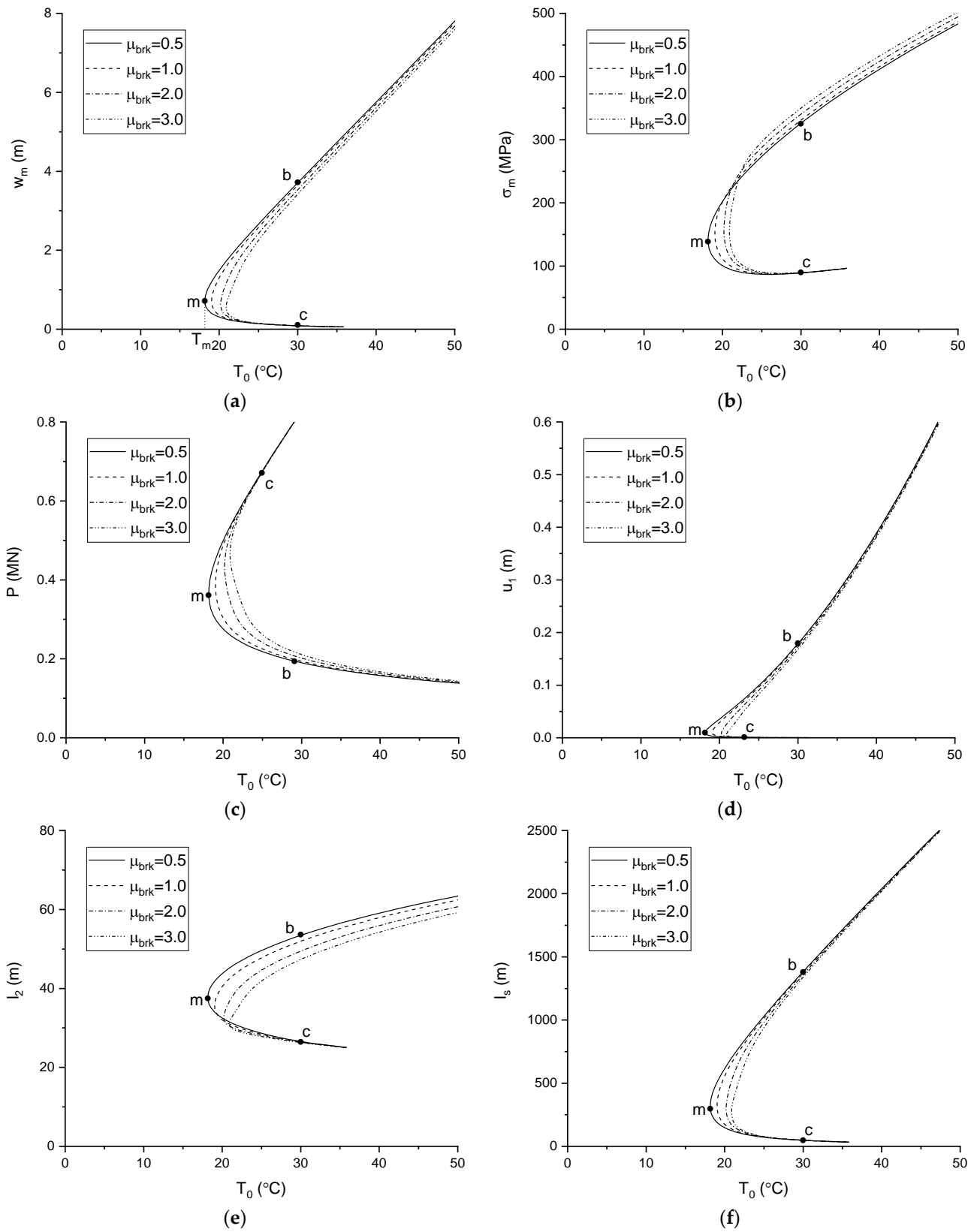


Figure 8. Influence of μ_{brk} on the buckling behaviour. (a) w_m . (b) σ_m . (c) P . (d) u_1 . (e) l_2 . (f) l_s ($v_{om} = 0.1$ m, $\mu_s = 0.1$).

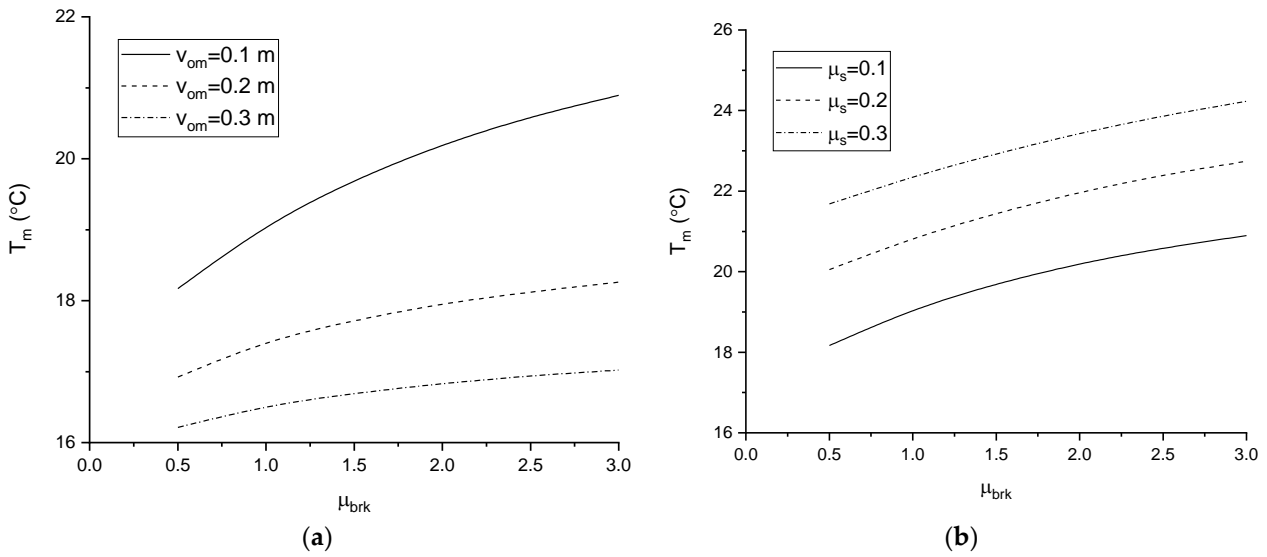


Figure 9. (a) Influence of μ_{brk} on T_m with different v_{om} ($\mu_s = 0.1$). (b) Influence of μ_{brk} on T_m with different μ_s . ($v_{om} = 0.1$ m).

However, P becomes larger with larger μ_{brk} (see Figure 8c). The reason for this is that the reduction in the axial force reduces, since the greater breakout resistance restricts the deflection of the buckled pipeline. Moreover, σ_m along the buckled pipeline becomes larger for larger μ_{brk} (see Figure 8b). After considering the nonlinear pipe–soil interaction model, both T_m and σ_m in the pipeline became larger. When the nonlinear pipe–soil interaction model is not included, lateral buckling may fail to be triggered by the sleeper, and the maximum stress along the buckled pipeline may exceed the allowable stress in the design.

3.2.2. Influence of v_{om}

The influence of v_{om} on the buckled configuration, post-buckling behaviour, and minimum critical temperature difference T_m are shown in Figures 10–12, respectively.

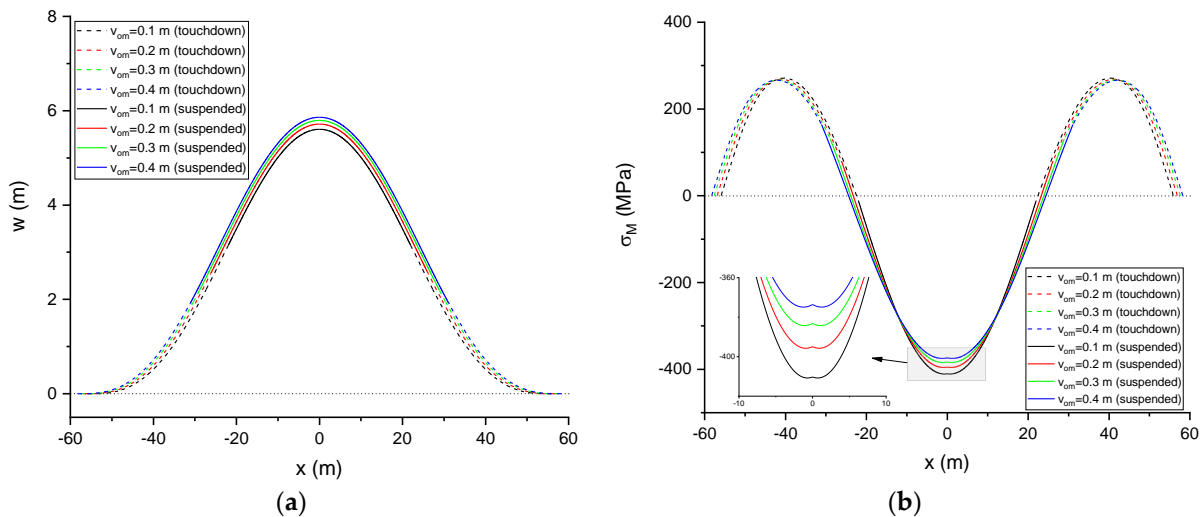


Figure 10. Influence of v_{om} on configurations. (a) Deformed shapes. (b) Bending stresses ($\mu_{brk} = 2.0$, $\mu_s = 0.1$, $T_0 = 40$ °C).

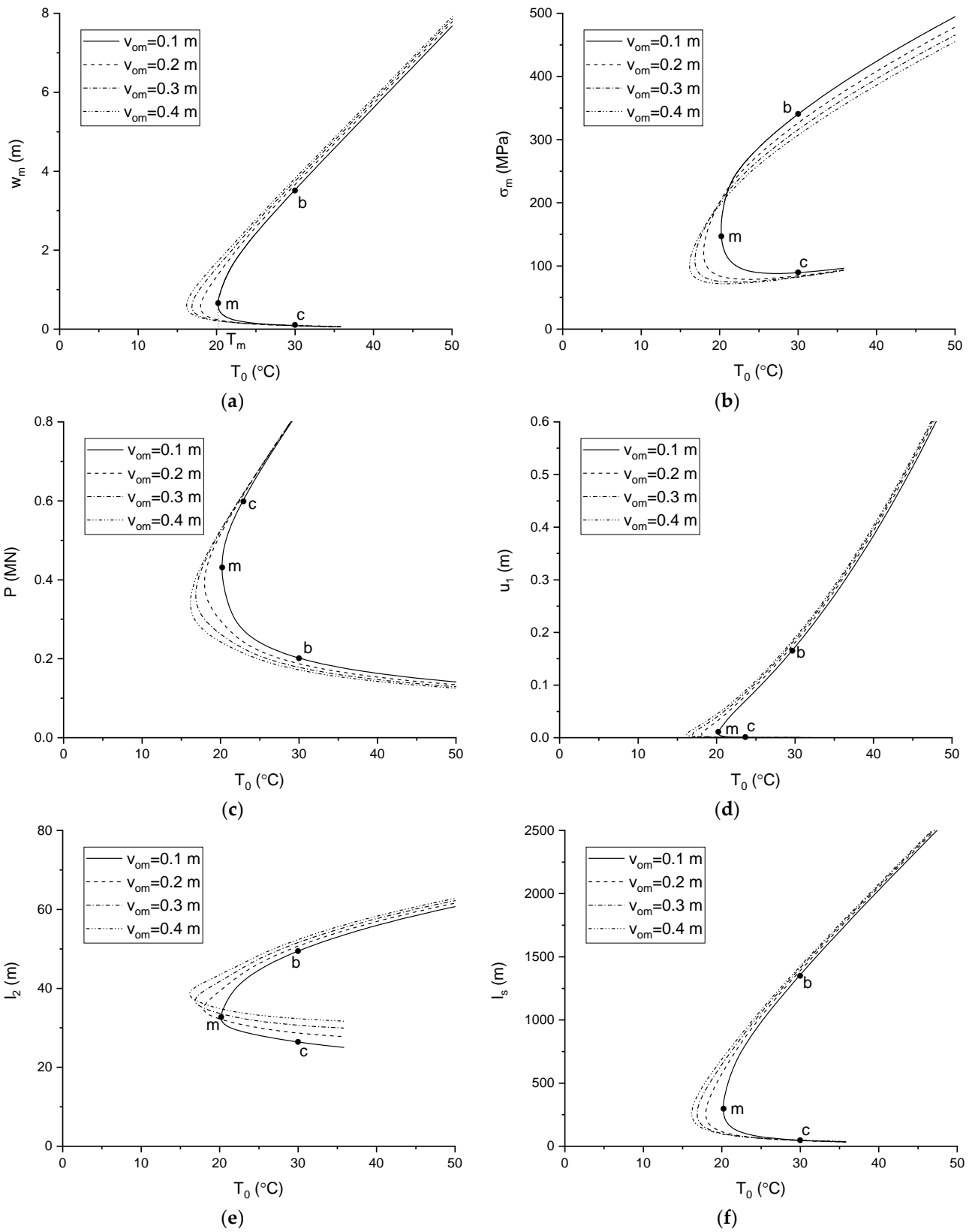


Figure 11. Influence of v_{om} on the buckling behaviour. (a) w_m . (b) σ_m . (c) P . (d) u_1 . (e) l_2 . (f) l_s ($\mu_{brk} = 2.0, \mu_s = 0.1$).

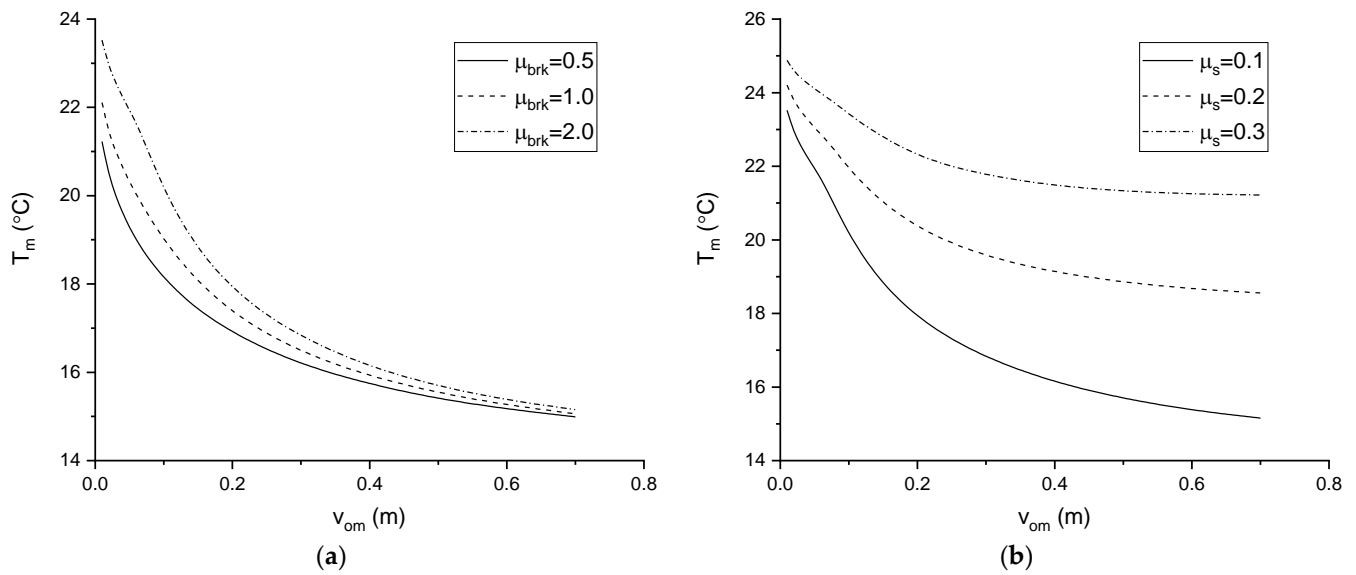


Figure 12. (a) Influence of v_{om} on T_m with different μ_{brk} ($\mu_s = 0.1$). (b) Influence of v_{om} on T_m with different μ_s ($\mu_{brk} = 2.0$).

From Figure 10a, it is clear that the length of the suspended pipe segment becomes larger with larger sleeper heights, v_{om} . The deflection of the buckled pipeline enlarges with larger v_{om} . Because the soil resistance for the suspended pipeline is zero, the buckled pipeline has less restriction from the seabed foundation with larger v_{om} . The deflection of the buckled pipeline enlarges with larger v_{om} , but both the local minimum and the local maximum (absolute value) of the bending stress become smaller with larger v_{om} , as shown in Figure 10b. This is because the deflection of the buckled pipeline is more benign with larger v_{om} .

In Figure 11a, T_m becomes smaller with larger v_{om} . Figure 12 illustrates the influence of v_{om} on T_m in detail. In Figure 12, T_m decreases with increasing v_{om} for specific values of μ_{brk} and μ_s , and the decreasing rate of T_m reduces with increasing v_{om} . In Figure 12a, under the same v_{om} , T_m becomes larger for larger μ_{brk} . The influence of μ_{brk} on T_m becomes smaller for larger v_{om} , since the length of suspended pipeline with zero soil resistance is greater. In Figure 12b, under the same v_{om} , T_m is larger with larger μ_s . The decreasing rate of T_m with increasing v_{om} becomes smaller with larger μ_s . The influence of μ_s on T_m is larger with larger v_{om} . The reason for this is that the concentrated contact force between the pipeline and the sleeper becomes larger with larger v_{om} , so that the friction force between the pipeline and the sleeper becomes larger with larger v_{om} . Therefore, an effective way to reduce T_m is to increase the sleeper height v_{om} ; however, the corresponding weakness is that the suspended pipeline will be longer, which may lead to vortex-induced vibration.

In Figure 11a,e, at a specific temperature difference, both w_m and l_2 become larger with larger v_{om} . This is because the length of the suspended pipeline with zero soil resistance increases with increasing v_{om} , as shown in Figure 10a. There is less restriction from the seabed foundation with larger v_{om} . Due to the larger deflection with larger v_{om} , the requirement of additional pipes to feed into the buckled section increases, which creates the need for more thermal expansion (see Figure 11d) and a longer feed-in region (see Figure 11f). The axial force P becomes smaller with larger v_{om} , since a larger deflection occurs to release more axial force, as shown in Figure 11c. The maximum stress σ_m along the buckled pipeline reduces with larger μ_{brk} (see Figure 11b).

3.2.3. Influence of μ_s

The influence of μ_s on the buckled configuration, post-buckling behaviour, and minimum critical temperature difference T_m are shown in Figures 13–15, respectively.

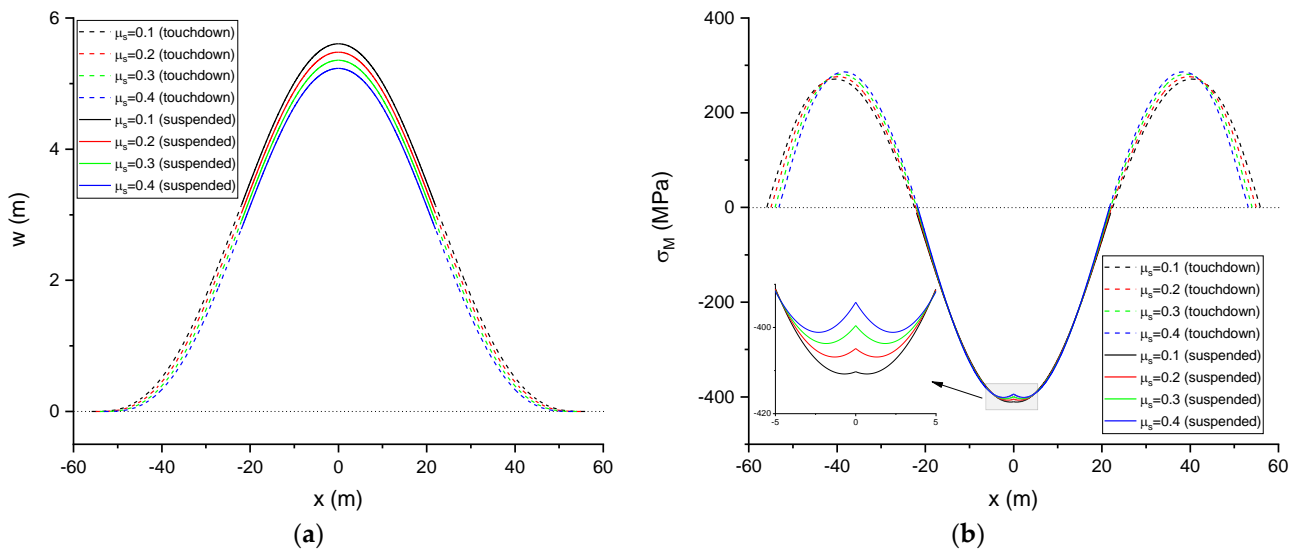


Figure 13. v_{om} on configurations. (a) Deformed shapes. (b) Bending stresses ($\mu_{brk} = 2.0$, $v_{om} = 0.1$ m, $T_0 = 40$ °C).

In Figure 13a, the deflection of the buckled pipeline shrinks with larger μ_s . This is because the friction force between the pipeline and the sleeper becomes larger with larger μ_s , which restricts the deflection of the buckled pipeline. In Figure 13b, the extrema of the bending stress in the positive direction becomes slightly larger with larger μ_s . However, both the local minimum and the local maximum (absolute value) of the bending stress close to the sleeper in the negative direction become smaller with larger μ_s , as shown in Figure 13b. With larger μ_s , the difference between the local minimum and the local maximum of the bending stress close to the sleeper becomes larger. Taking $\mu_s = 0.4$ as an example, it is clear that the local minimum (absolute value) of the bending stress is smaller than the local maximum (absolute value) of the bending stress.

In Figure 14a, T_m is larger with larger μ_s . The effect of μ_s on T_m is illustrated in Figure 15, with different values of μ_{brk} and v_{om} . In Figure 15, T_m increases with increasing μ_s for specific values of μ_{brk} and v_{om} , and the increasing rate of T_m slightly reduces with increasing μ_s . The friction force between the sleeper and the pipeline becomes larger with larger μ_s , which makes it more difficult to trigger the lateral buckling. In Figure 15a, at the same μ_s , T_m becomes larger with larger μ_{brk} . The increasing rate of T_m with increasing μ_s is similar for different values of μ_{brk} . In Figure 15b, under the same μ_s , T_m becomes smaller for larger v_{om} . The increasing rate of T_m with increasing μ_s is larger for larger v_{om} . The influence of v_{om} on T_m gradually reduces with increasing μ_s . Thus, the friction coefficient between the sleeper and the pipeline μ_s should be carefully controlled. When the value of μ_s is too large, such as $\mu_s = 0.6$, T_m is barely affected by the sleeper height v_{om} .

In Figure 14a,e, under a specific T_0 , both w_m and l_2 reduce with larger μ_s . This is because, since the friction force between the sleeper and the pipeline becomes larger with larger μ_s , the deflection of the buckled pipeline is restricted by the larger resistance between the sleeper and the pipeline. Thus, the requirements of both u_1 and l_s decrease with larger μ_s , as shown in Figure 14d,f. Due to the restriction of the larger friction force between the sleeper and the pipeline, the axial force P increases with increasing μ_s , as shown in Figure 14c. However, the maximum stress σ_m along the buckled pipeline reduces with larger μ_s (see Figure 14b), which is induced by the decrease in the maximum bending stress (absolute value) along the buckled pipeline.

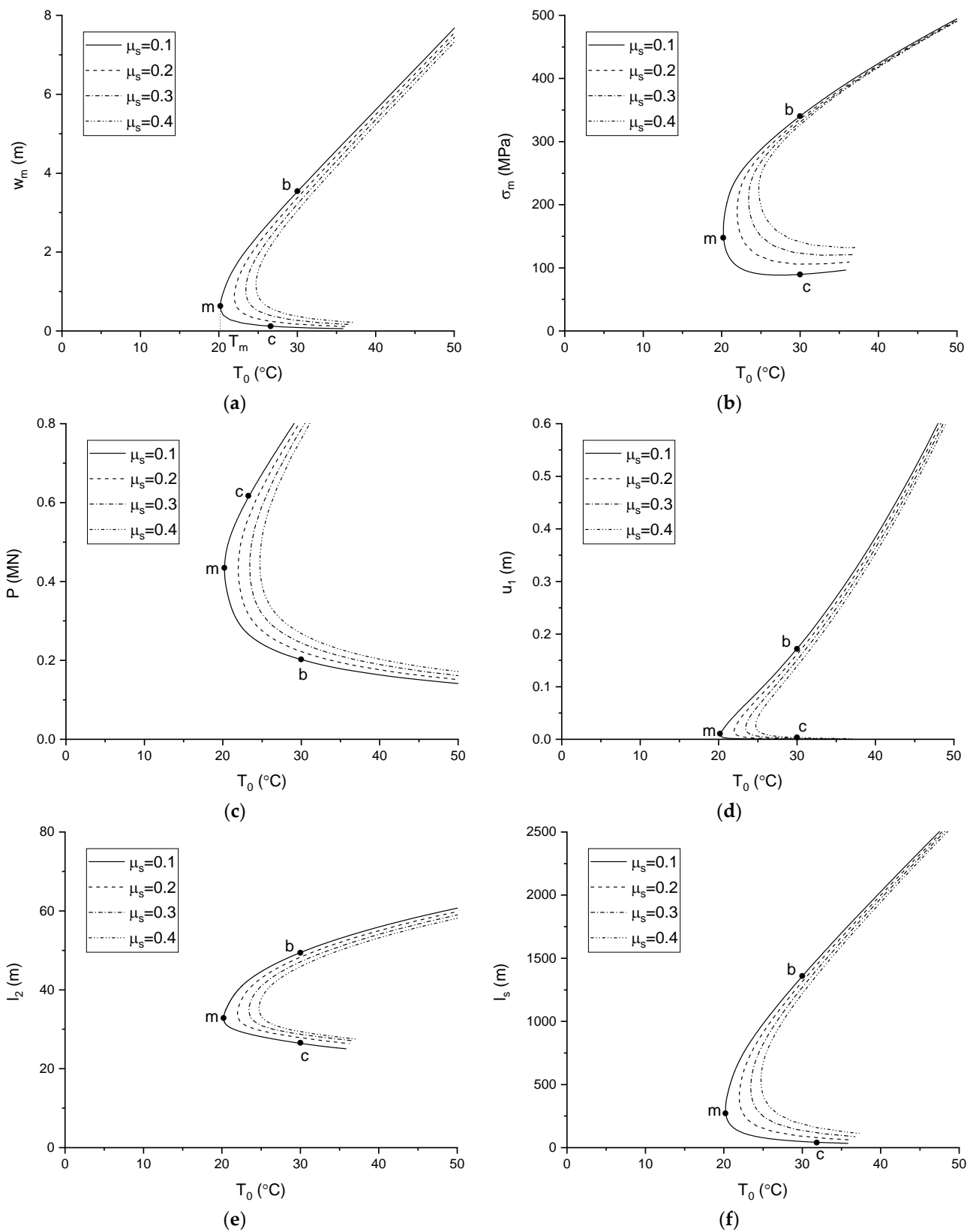


Figure 14. Influence of μ_s on the buckling behaviour. (a) w_m . (b) σ_m . (c) P . (d) u_1 . (e) l_2 . (f) l_s ($\mu_{brk} = 2.0, v_{om} = 0.1$ m).

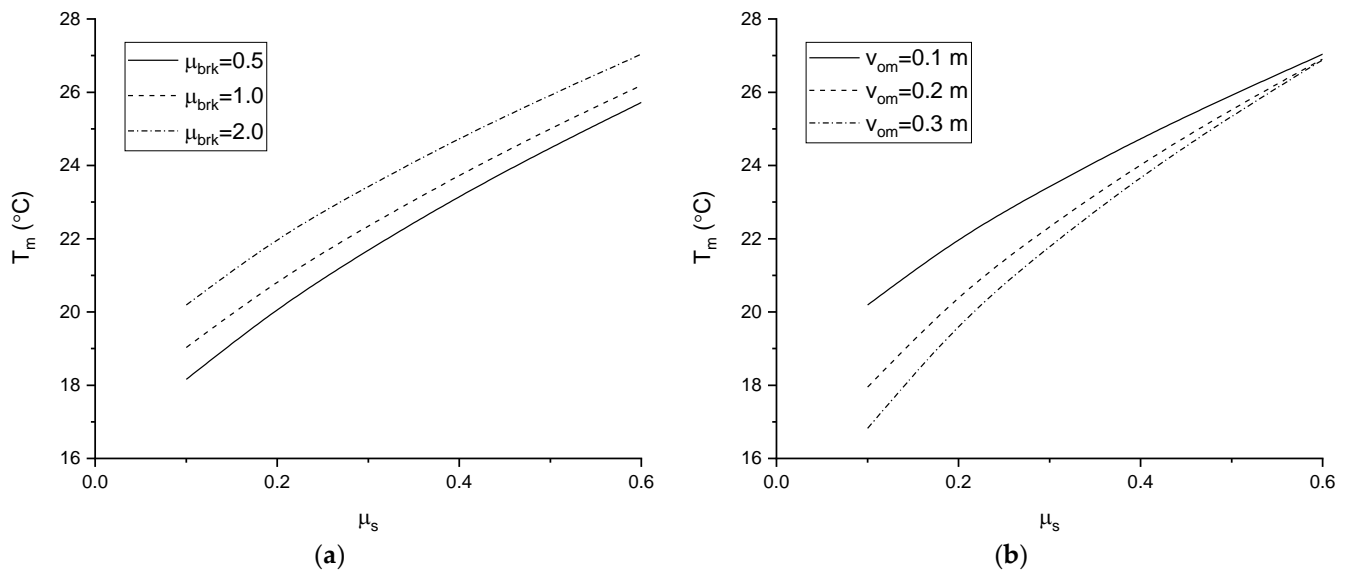


Figure 15. (a) Influence of μ_s on T_m with different μ_{brk} ($v_{om} = 0.1$ m). (b) Influence of μ_s on T_m with different v_{om} ($\mu_{brk} = 2.0$).

4. Conclusions

Through a consideration of the nonlinear pipe–soil interaction model, a mathematical model was proposed to simulate the lateral buckling of subsea pipelines triggered by a sleeper. The model was solved numerically and validated by comparing its predictions with the analytical solutions from [26]. The discrepancy between the numerical and analytical solutions was analysed through the discussion of the mobilization distance. A detailed parametric analysis was presented to show the effect of the breakout resistance, sleeper height, and sleeper friction coefficient on the buckling behaviour of a pipeline laid on a sleeper. The conclusions are:

- (i) The discrepancy between the numerical and analytical solutions comes from the difference between the elastic-plastic and rigid-plastic pipe–soil interaction models, which reduces with decreasing mobilization distance in the elastic-plastic pipe–soil interaction model.
- (ii) When the nonlinear pipe–soil interaction model is taken into account, both the displacement amplitude and the buckled length reduce due to the occurrence of breakout resistance, which decreases further with increasing breakout resistance. However, both the axial force and the maximum stress, along with the buckled pipeline, increase, and increase further with increasing breakout resistance.
- (iii) The deflection of the buckled pipeline enlarges as the sleeper height increases and shrinks as the sleeper friction coefficient increases. The axial force decreases with increasing sleeper height and increases with increasing sleeper friction coefficient. Moreover, the maximum stress along the buckled pipeline decreases with increasing sleeper height and with decreasing sleeper friction coefficient.
- (iv) The minimum critical temperature difference increases with increasing breakout resistance and sleeper friction coefficient, and decreases with increasing sleeper height. The influence of the breakout resistance on the minimum critical temperature difference gradually reduces with increasing sleeper height. Moreover, the sleeper height has little effect on the minimum critical temperature difference when the sleeper friction coefficient is large enough.

In conclusion, it is better to incorporate the nonlinear pipe–soil interaction model into the mathematical model when simulating the lateral buckling of subsea pipelines triggered by a sleeper, since both the minimum critical temperature difference and the maximum

stress increase. Moreover, both the sleeper height and the sleeper friction coefficient should be carefully selected and controlled.

Author Contributions: Conceptualization, Z.W. and C.G.S.; methodology, Z.W.; software, Z.W.; validation, Z.W.; investigation, Z.W.; writing—original draft preparation, Z.W.; writing—review and editing, C.G.S.; supervision, C.G.S.; project administration, C.G.S.; funding acquisition, C.G.S. All authors have read and agreed to the published version of the manuscript.

Funding: Zhenkui Wang would like to acknowledge that the work described in this paper was funded by the National Natural Science Foundation of China (grant number: 52001229). This work contributes to the Strategic Research Plan of the Centre for Marine Technology and Ocean Engineering (CENTEC), which is financed by the Portuguese Foundation for Science and Technology (Fundação para a Ciência e Tecnologia—FCT) under contract UIDB/UIDP/00134/2020.

Institutional Review Board Statement: Not applicable.

Informed Consent Statement: Not applicable.

Data Availability Statement: Not applicable.

Conflicts of Interest: The authors declare no conflict of interest.

References

1. DNV-RP-F110; Global Buckling of Submarine Pipelines. Det Norske Veritas: Oslo, Norway, 2019.
2. Hobbs, R.E. In-service buckling of heated pipelines. *J. Transp. Eng.* **1984**, *110*, 175–189. [[CrossRef](#)]
3. Taylor, N.; Gan, A.B. Submarine pipeline buckling-imperfection studies. *Thin-Walled Struct.* **1986**, *4*, 295–323. [[CrossRef](#)]
4. Croll, J.G.A. A simplified model of upheaval thermal buckling of subsea pipelines. *Thin-Walled Struct.* **1997**, *29*, 59–78. [[CrossRef](#)]
5. Karampour, H.; Albermani, F.; Veidt, M. Buckle interaction in deep subsea pipelines. *Thin-Walled Struct.* **2013**, *72*, 113–120. [[CrossRef](#)]
6. Liu, R.; Xiong, H.; Wu, X.; Yan, S. Numerical studies on global buckling of subsea pipelines. *Ocean Eng.* **2014**, *78*, 62–72. [[CrossRef](#)]
7. Hong, Z.; Liu, R.; Liu, W.; Yan, S. Study on lateral buckling characteristics of a submarine pipeline with a single arch symmetric initial imperfection. *Ocean Eng.* **2015**, *108*, 21–32. [[CrossRef](#)]
8. Liu, R.; Wang, X. Lateral global buckling high-order mode analysis of a submarine pipeline with imperfection. *Appl. Ocean. Res.* **2018**, *73*, 107–126. [[CrossRef](#)]
9. Konuk, I. Coupled lateral and axial soil-pipe interaction and lateral buckling Part II: Solutions. *Int. J. Solids Struct.* **2018**, *132–133*, 127–152. [[CrossRef](#)]
10. Konuk, I. Coupled lateral and axial soil-pipe interaction and lateral buckling Part I: Formulation. *Int. J. Solids Struct.* **2018**, *132–133*, 114–126. [[CrossRef](#)]
11. Zhang, X.; Duan, M. Prediction of the upheaval buckling critical force for imperfect submarine pipelines. *Ocean Eng.* **2015**, *109*, 330–343. [[CrossRef](#)]
12. Zhang, X.; Guedes Soares, C.; An, C.; Duan, M. An unified formula for the critical force of lateral buckling of imperfect submarine pipelines. *Ocean Eng.* **2018**, *166*, 324–335. [[CrossRef](#)]
13. Liu, R.; Li, C. Determinate dimension of numerical simulation model in submarine pipeline global buckling analysis. *Ocean Eng.* **2018**, *152*, 26–35. [[CrossRef](#)]
14. Zeng, X.; Duan, M. Mode localization in lateral buckling of partially embedded submarine pipelines. *Int. J. Solids Struct.* **2014**, *51*, 1991–1999. [[CrossRef](#)]
15. Chee, J.; Walker, A.; White, D. Effects of variability in lateral pipe-soil interaction and pipe initial out-of-straightness on controlled lateral buckling of pre-deformed pipeline. *Ocean Eng.* **2019**, *182*, 283–304. [[CrossRef](#)]
16. Zhang, X.; Guedes Soares, C. Lateral buckling analysis of subsea pipelines on nonlinear foundation. *Ocean Eng.* **2019**, *186*, 106085. [[CrossRef](#)]
17. Peek, R.; Yun, H. Flotation to trigger lateral buckles in pipelines on a flat seabed. *J. Eng. Mech.* **2007**, *4*, 442–451. [[CrossRef](#)]
18. Shi, R.; Wang, L. Single buoyancy load to trigger lateral buckles in pipelines on a soft seabed. *J. Eng. Mech.* **2015**, *141*, 1–7. [[CrossRef](#)]
19. Wang, Z.; Tang, Y. Antisymmetric thermal buckling triggered by dual distributed buoyancy sections. *Mar. Struct.* **2020**, *74*, 102811. [[CrossRef](#)]
20. Chee, J.; Walker, A.; White, D. Controlling lateral buckling of subsea pipeline with sinusoidal shape pre-deformation. *Ocean Eng.* **2018**, *151*, 170–190. [[CrossRef](#)]
21. Silva-Junior, H.C.; Cardoso, C.O.; Carmignotto, M.A.P.; Zanutto, J.C. Reduced Model Device of Solutions to Control Thermal Buckling Effects in HP-HT Subsea Pipelines (OMAE2008-57637). In Proceedings of the International Conference on Ocean, Offshore and Arctic Engineering, Estoril, Portugal, 15 June 2008.

22. de Oliveira Cardoso, C.; Solano, R.F. Performed of triggers to control thermal buckling of subsea pipelines using reduced scale model (ISOPE-I-15-445). In Proceedings of the International Offshore and Polar Engineering Conference, Honolulu, HI, USA, 21–26 June 2015.
23. Bai, Q.; Qi, X.; Brunner, M. Global buckle control with dual sleepers in HP/HT pipelines (OTC-19888-MS). In Proceedings of the Offshore Technology Conference, Houston, TX, USA, 4–7 May 2009.
24. Wang, Z.; Tang, Y. Analytical study on controlled lateral thermal buckling of antisymmetric mode for subsea pipelines triggered by sleepers. *Mar. Struct.* **2020**, *71*, 102728. [[CrossRef](#)]
25. Hong, Z.; Liu, W. Modelling the vertical lifting deformation for a deep-water pipeline laid on a sleeper. *Ocean Eng.* **2020**, *199*, 107042. [[CrossRef](#)]
26. Wang, Z.; Tang, Y.; van der Heijden, G.H.M. Analytical study of lateral thermal buckling for subsea pipelines with sleeper. *Thin-Walled Struct.* **2018**, *122*, 17–29. [[CrossRef](#)]
27. Lagrange, R.; Averbuch, D. Solution methods for the growth of a repeating imperfection in the line of a strut on a nonlinear foundation. *Int. J. Mech. Sci.* **2012**, *63*, 48–58. [[CrossRef](#)]
28. Wang, Z.; Tang, Y.; van der Heijden, G.H.M. Analytical study of distributed buoyancy sections to control lateral thermal buckling of subsea pipelines. *Mar. Struct.* **2018**, *58*, 199–222. [[CrossRef](#)]
29. Chatterjee, S.; White, D.J.; Randolph, M.F. Numerical simulations of pipe-soil interaction during large lateral movements on clay. *Géotechnique* **2012**, *62*, 693–705. [[CrossRef](#)]
30. *Wolfram Mathematica*, version 11.0; Wolfram Research, Inc.: Champaign, IL, USA, 2016.